Calculating the Probability of Injected Carbon Dioxide Plumes Encountering Faults

Preston D. Jordan[1*], Curtis M. Oldenburg[1] and Jean-Philippe Nicot[2]

[1]Earth Sciences Division
Lawrence Berkeley National Laboratory
Berkeley, California 94720

[2]Bureau of Economic Geology
Jackson School of Geosciences
University of Texas
Austin, Texas 78713

Abstract

One of the main concerns of storage in saline aquifers is leakage via faults. In the early stages of site selection, site-specific fault coverages are often not available for these aquifers. This necessitates a method using available fault data to estimate the probability of injected carbon dioxide encountering and migrating up a fault. The probability of encounter can be calculated from areal fault density statistics from available data, and carbon dioxide plume dimensions from numerical simulation. Given a number of assumptions, the dimension of the plume perpendicular to a fault times the areal density of faults with offsets greater than some threshold of interest provides probability of the plume encountering such a fault. Application of this result to a previously planned large-scale pilot injection in the southern portion of the San Joaquin Basin yielded a 3% and 7% chance of the plume encountering a fully and half seal offsetting fault, respectively. Subsequently available data indicated a half seal-offsetting fault at a distance from the injection well that implied a 20% probability of encounter for a plume sufficiently large to reach it.

[*] Corresponding author: E-mail: pdjordan@lbl.gov; phone: (510) 486-6774; Fax: (510) 486-5686

Introduction

The potential for leakage of CO_2 via fault zones is an area of considerable uncertainty for geological storage of CO_2 (Benson and Cook 2005). This uncertainty exists with regard to the probability and the consequences of leakage, key concerns for risk assessment of geological CO_2 storage (e.g., Oldenburg et al., 2009). The probability of leakage via faults can be segmented into two parts: the probability of encountering a fault and the probability of flow along the fault out of the storage target.

Fault zone flow and transport properties vary considerably, with some fault zones forming recognized conduits for fluid flow, as commonly evidenced by springs co-located with fault zones, and others forming barriers to fluid flow, as evidenced by many hydrocarbon reservoirs created in part by sealing faults. There is currently little consensus regarding a methodology for characterizing fault zone flow and transport properties in the deep subsurface.

In contrast, research regarding fault population statistics has reached a moderate level of consensus. While there are certainly more questions and unsettled issues in this field, it is sufficiently mature to be constructively applied to the concern regarding fault zone leakage of CO_2 from prospective storage reservoirs.

This study utilizes the findings of fault population research to develop an approach for estimating the probability of a CO_2 plume encountering a fault. The intent of the approach is to provide an estimate of whether fault leakage requires further analysis at a proposed site for which sufficient data are lacking (such as seismic reflection data) to allow a more deterministic analysis. The approach can provide useful data during the early phases of site selection or risk assessment, although it obviously sidesteps the issue of whether CO_2 will flow along a specific fault zone after encounter. Theoretically, at some prospective sites the probability of a plume

encountering a fault is so low as to not warrant the more complicated measurement and/or estimation of fault zone properties. The approach described here is one of the specialized models developed for the risk assessment framework described in Oldenburg et al. (2009). We note further that although the emphasis here is on CO_2 leakage, the approach is general and can be applied to estimate the probability of displaced brine encountering a fault and the probability that a pressure increase above a selected threshold will encounter a fault.

Fault Encounter Probability Estimation

The proposed analysis of the probability of a CO_2 plume encountering a fault proceeds by the following steps, which are expanded upon below. Note that for relatively symmetric plumes, the fault and plume orientation, and plume aspect ratio can be ignored. This might occur in relatively homogeneous flat-lying storage targets for instance.

1) Identify fault coverage(s) (fault-map data) relevant to a proposed site.
2) Measure fault lengths, orientations, and displacements from the coverage(s).
3) Define fault orientation modes through plotting and/or statistical analysis.
4) Analyze spatial trends in *F* and select data set applicable to proposed site.
5) Calculate *F* at various *d* and plot in log-log and semi-log space.
6) Model *F* versus *d* distribution.
7) Estimate plume area, aspect ratio and orientation (via analytical or numerical means).
8) Calculate the encounter probability at the *d* of interest from site-specific *F*-distribution model, fault orientation modes, and plume area, aspect ratio, and orientation.

The given approach utilizes *F*, whereas fault population research has focused on other parameters, such as the number of faults greater than a particular length, or the number of scan

line intersections with faults having greater than a particular displacement, N_d. F is easier to work with as it avoids the confounding effects of fault intersections and introduction of bias by fault coverage boundary orientation. F is proportional to N_d, as shown in the companion paper Jordan et al. (2011), and so with adjustment of the proportionality constant F can be substituted for N_d into the relevant equations developed by fault population researchers. This allows application of many fault population research results in the following, such as Step 6.

The fault encounter estimation steps, with the exception of steps 3 and 7, are discussed in more detail below. Discussion of step 3 is omitted because it is common practice and discussion of step 7 is omitted because it is beyond the scope of this paper.

Fault Coverage(s), Measurements, Calculations, And Density Trend Analysis (Steps 1, 2, 4 and 5)

Fault coverage(s) relevant to a proposed site can consist of oil or gas field structure maps, gas storage facility structure maps, or regional geologic maps, given analysis showing their relevance to the storage target. After identification of these coverages, fault segment lengths, orientations and displacements, and the area of the coverage are measured. Segment boundaries occur where a displacement value is available or where the fault orientation changes more than the desired precision.

In the case of initial site screening, fault coverages may not be available for the storage target. In this case, the applicability of the fault coverages to the storage target can be tested if a number of different coverages in relation to the storage target are available. Uniformity or trends in F with vertical, horizontal, and stratigraphic position can inform the selection of the results measured from the fault coverages that are applicable to the proposed storage target. This analysis may need to proceed iteratively with plotting of F versus d in step 5. This is particularly

true if the source coverages have different resolution limits, in which case plotting *F* versus *d* for each coverage allows comparing *F* for the same *d* across all coverages. The resolution limit is the minimum *d* for which the fault coverage includes all or almost all faults.

To calculate *F* for a given displacement cutoff, *d*, the total length of the fault segments with displacement greater than *d* must be calculated and divided by the coverage area. *F* is plotted against *d* in semi-log and log-log space to develop an understanding of the fault population.

Fault Density Distribution Modeling (Step 6)

Corrections can be applied to the measured *F* versus *d* distribution to compensate for the bias introduced by the resolution limit and the limited spatial extent of the coverage used (finite range effect) (Pickering et al. 1995). A numerical expression is developed for the observed relationship. These expressions are typically exponential, power-law or characteristic reflecting the development of the fault network, which in turn results from the amount of strain. These expressions can be used to extend the range of *F* versus *d* to values of *d* below the resolution limit of the map (termed d_m, the minimum throw resolution; Pickering et al. 1995).

Calculating Plume Fault Encounter Probability (Step 8)

The approach to calculating the probability of a plume encountering a fault (an event *g*) is based on simple two-dimensional geometric arguments and concepts of fault displacement cutoff. This approach is taken with full knowledge that measurements of fault population distributions from two-dimensional coverages (maps or sections) are biased relative to the population distribution in three dimensions (Marrett and Allmendinger 1991). However, because the CO_2 plumes resulting from commercial injections in individual reservoirs will typically be

"thin" (high length to thickness ratios) due to both the volume of the CO_2 injected versus the reservoir geometry as well as the buoyancy of CO_2 relative to water/brine, the approach seems reasonable.

The two-dimensional assumption also places the focus on the length of a fault encountered by a plume rather than the area of a fault so encountered. This necessitates that the offset of an actual fault encountered by an actual, three-dimensional plume does not vary considerably over the depth of the plume. This is reasonable for faults that have a vertical extent significantly larger than the thickness of the plume. The minimum length of such faults would still be small relative to the length of the plume, though, due to the aforementioned large aspect ratio of the plume, so the assumption of constant fault displacement across the plume is reasonable for all but very small faults.

In Figure 1, A_o is some large area within which the plumes are randomly centered, and L is the length of the fault in that area. If a circular plume is centered within a radius of the fault, it will encounter the fault. Figure 2 shows the area A_f within which this will occur. Figure 2 indicates that in general the probability of g is given by

$$\Pr(g) = \frac{A_f}{A_0} \qquad (1).$$

This approach assumes that each hypothetical plume encounters one fault at most, and that the fault entirely transects the plume when encountered. With this assumption, if a plume is centered within a plume radius, r, of a fault, g will occur. Given that the fault has two sides

$$A_f = 2rL \qquad (2).$$

L can also be written as the areal fault density F times A_o:

$$L = FA_0 \quad (3).$$

Substituting Equation 3 into 2, 2 into 1, and canceling terms gives

$$\Pr(g) = 2rF \quad (4).$$

If the plume margin is some shape other than circular, then Equation 4 can be generalized to any plume shape by substituting half the plume dimension perpendicular to the fault, *k*:

$$\Pr(g) = 2kF \quad (5).$$

The value of *k* can be measured directly from plots of the expected area swept by mobile CO2 generated by numerical simulations or possibly calculated by analytical or semi-analytical methods. Alternately, using the plume area from one of these methods, the plume can be approximated as an ellipse and *k* calculated from the fault orientation, plume aspect ratio and plume orientation according to the method in Appendix 1. This has the advantage of allowing exploration of the consequences of different plume geometries, such as due to uncertainty in the orientation and magnitude of horizontal permeability anisotropy.

Due to the assumptions, this method is only useful for plumes with fault-perpendicular dimensions considerably smaller than the average spacing between the faults of interest. As the fault-perpendicular plume dimension approaches the distance between faults (the fault spacing), this method will overestimate Pr(*g*) because the chance a plume will encounter two faults will be non-negligible. This error just over 10% for Pr(*g*) equal to 0.10, presuming randomly distributed faults. The error is approximately 25% for Pr(*g*) equal to 0.20. However these errors are not particularly significant as either of these values of Pr(*g*) indicate fault flow and transport properties should be carefully considered and characterized during project planning. It is only at

Pr(g) values of 0.01 or less where fault flow and transport properties start to be of less over riding initial concern, and so precision in the Pr(g) calculation matters. The approach presented in this paper provides that precision. For instance, the error is approximately 1% for a Pr(g) equal to 0.01 and decreases with smaller Pr(g).

Case Study: The Kimberlina Phase III Pilot Test

WESTCARB's Kimberlina Phase III pilot test project is located in the southern San Joaquin Basin in California about 27 km (17 mi.) northwest of Bakersfield, as shown on Figure 3. The San Joaquin Basin extends about 350 km (220 mi.) from the Stockton Arch to its southern terminus at the northern Transverse Ranges and averages 80–110 kilometers (50–70 miles) wide. It is bounded on the east by the Sierra Nevada and on the west by the Coast Ranges (NETL 2009). During the Mesozoic, the area was a fore-arc basin during subduction of the Farallon plate. By middle Tertiary time, the basin had become relatively isolated as a result of the transpressional margin that followed the passage of the Mendocino triple junction. The depositional environment generally progressed from deep marine in the Mesozoic to alluvial at present with a number of intervening transgression-regression sequences (Graham and Williams 1985).

During the Kimberlina Phase III pilot test, 1 Mt (10^6 t = 10^9 kg; $1.1*10^6$ T = $2.2*10^9$ lbs) of CO_2 is planned for injection into the Vedder sandstones over four years (NETL 2009). The Vedder consists of interbedded sandstones and shales deposited on the marine slope, shelf and delta comprising a ramp (Bloch 1986). At the site, the Vedder has a thickness up to 160 m (520 ft), and occurs at a depth of 2,300 m (7,500 ft) (Wagoner 2009). Thick continuous shale units

provide good overlying seals at the site and surrounding areas (Wagoner 2009). Faults in the vicinity appear to be primarily growth faults (McPherson 1978).

Fault Coverages (Step 1)

Little data on faults at the Kimberlina site is publicly available. However, structure maps for the surrounding oil and gas fields shown in Figure 4 are available in Volume 1 of "California Oil and Gas Fields" by the California Division of Oil, Gas and Geothermal Resources (DOGGR 1998).

Measure Fault Orientation, Length and Displacement (Step 2)

Fault orientations, lengths and throws (vertical offset), as well as map areas, were measured from the structure maps for the fields shown in Figure 4 (with the exception of the Rose Field for which no data were available). Figure 5 shows one of the structure maps.

The orientation and length of 956 fault segments were measured. Throws were measured at 1,029 points. The total fault length measured was 465 km (289 mi). These measurements are discussed further in Jordan et al. (2011).

Fault Orientation Modes (Step 3)

Faults in oil fields centered within 16 km (10 mi.) of the Kimberlina site strike primarily north to north by northwest. Faults in oil fields centered from 16 km (10 mi.) to 24 km (15 mi.) of the Kimberlina site occur in three orientation modes. In order of dominance they are northwest, northeast and north. These are further depicted and discussed in Jordan et al. (2011). The predominant fault strike of 350° in fields centered within 16 km (10 mi.) of the Kimberlina was used for the probability calculation.

Analyze Spatial Trends in F and Select Applicable Data Set (Step 4)

Analysis of fault density variation across the geologic section indicates it does not vary considerably through the section containing the structural surfaces in the data set. This is discussed further in Jordan et al. (2011).

Figure 4 shows there is only one field centered in the quadrant north of the Kimberlina site, and so little fault density data from this quadrant was available for this study. The fault density in fields centered from the northeast to southwest was higher on average than in those centered from the southwest to northwest. Unlike fault orientation, though, there is no obvious trend in fault density with distance. These findings are explained in more detail in Jordan et al. (2011).

These results suggest the Kimberlina site is in a transitional area between higher and lower fault densities, and so the fault densities from all the fields were aggregated for this study. As more fields exist in the quadrants with higher average density, it may be that the density aggregate from the fields overestimates the fault density in the vicinity of Kimberlina. This would lead to a higher than actual estimate of fault encounter probability.

Calculate And Plot F Versus d (Step 5)

Figure 6 shows the raw *F* versus *d*. Selection of the *d* bins proceeded iteratively with the next step.

Model F Versus d Distribution (Step 6)

It is tempting to see the raw *F* versus *d* distribution in Figure 6 as exponential given the good fit to the data, but low displacement faults are always underreported due to the fault

mapping resolution limit (Pickering et al. 1995). As a result, the actual fault population is always larger than the measured data at the low end of the range. Additionally, the spatial limitation of the coverages relative to the fault network they map introduces additional bias (Pickering et al. 1995).

Accounting for these effects yields the more appropriate fault density distribution model shown on Figure 7. This is a power-law model based upon the data above the resolution limit corrected for the spatial limits of the coverages using an approach suggested by Pickering et al. (1995). Modeling of the fault density distribution is further discussed in Jordan et al. (2011).

CO_2 Plume Simulation (Step 7)

The anticipated CO_2 plume at the Kimberlina site was numerically simulated using the ECO2N equation of state package of TOUGH2 (Pruess and Garcia 2002). The model simulated the injection of 250,000 t/yr of CO_2 for four years, then simulated migration and trapping of the plume over the next 46 years. Figure 8 shows CO_2 saturation and saturation above residual saturation at several time steps in the numerical modeling. Saturation above residual is referred to as the mobile fraction. On Figure 8, zero is no saturation above residual, and one is 100% saturation.

The area within the outer contour on the last frame of Figure 8 is the region swept by CO2 since the start of injection. This area changes little after 30 years, and so is termed the "plume area" for the purposes of analyzing the probability of mobile CO_2 encountering a fault. This definition of the plume area differs from other possible definitions, such as the area swept by dissolved CO_2.

Fault Encounter Probability (Step 8)

For Kimberlina, the plume area, as measured from Figure 8, is 0.83 km^2 (0.32 mi^2). The throw truncation is selected for relevance to potential leakage of CO_2. As a first approximation, throws that fully offset the sealing formations over the target reservoirs are of concern. The sealing formations over the Vedder have a vertical thickness of approximately 180 m (600 ft). The corrected fault density equation on Figure 7 indicates the average fault density at this throw truncation is 0.028 km/km^2 (0.046 $mi./mi.^2$). This is a low density, so the condition that the fault-perpendicular plume dimension is much smaller than the spacing between faults is sufficiently met to use the probability estimation method.

The half dimension of the plume perpendicular to the predominant fault strike near the Kimberlina site is 0.58 km (0.36 mi.). Given this length and the fault density above, Equation 5 indicates the probability of the numerically simulated plume encountering a fully seal-offsetting fault is 3.2%.

The numerical model did not incorporate the effect of the fault zones on the bulk phase CO_2 flow, however. As indicated by the corrected power-law distribution in Figure 7, the density of smaller offset faults is probably quite high. For instance, at a throw cutoff of 3 m (10 ft), the density is approximately 3 km/km^2 (5 $mi./mi.^2$). Despite their small offset, the permeability in these fault zones will likely contrast with that of the host rock. Given their high density, it is likely the plume will encounter these small faults and be deflected somewhat to the north. These faults are likely to cause greater elongation of the plume compared to the numerical model results as well.

Approximating the plume footprint of the mobile fraction as an ellipse with the same area as the numerically simulated plume allows application of the method in Appendix 1 to explore

the impact of this possible anisotropy on fault encounter probability. Some results of this approach for a fully-seal offsetting fault are given in Table 1. Figure 9 shows the results of this approach.

The simulated plume had an aspect ratio of 1.32 and its axis was oriented 70° to the predominant fault orientation. This point is indicated on Figure 9 and matches the 3.2% probability given above. Accounting for anisotropy due to small faults, a plume aspect ratio of two and an acute angle between the plume axis and the faults of 35° is perhaps more typical. As indicated on Figure 9, the fault encounter probability of such a plume is 2.9%.

Table 2 and Figure 10 provide the probability of the Kimberlina plume encountering a fault that offsets the seal at least halfway (90 m [300 ft]). The probability of the modeled plume encountering such a fault is 7%. This is provided not because such faults are particularly significant, but rather to provide some feel for the variation in probability with variation in throw truncation.

Outcome

At the time of the analysis presented above, a structural model of the Kimberlina site had been constructed from publicly available well logs and proprietary seismic picks provided by EOG resources, Inc. (Wagoner 2009). A northwest striking fault was interpreted northeast of the injection site from the seismic data, but uncertainty about it prevented it from being included explicitly in the geologic model available during this study. Additional reports concerning faulting in the area (Los Angeles Department of Water and Power, 1974; Holzer, 1980; Smith, 1983) were subsequently located. These reports indicated the presence of the northwest striking Pond Fault northeast of the site. These sources allowed a more detailed interpretation of well log

data, leading to interpretation of the Pond Fault passing through the Vedder Formation about 2.8 km (1.7 mi.) northeast of the site with an offset of about half the seal thickness (Wagoner 2009).

From Figure 8, the plume extends 1 km (0.62 mi.) to the northeast toward the fault from the injection well. Consequently, the new fault interpretation suggests that a half seal-offsetting fault does not occur within the modeled plume footprint, which is in accord with the 7% encounter probability respectively. However if the plume were in the same orientation but 2.8 times the length of that modeled, the encounter probability would rise to 20% for a half seal offsetting fault using the methodology presented, and in fact the recent result suggests this plume would encounter such a fault. These are single point outcomes of course, and consequently they provide only the barest beginning of the retrospective data necessary to validate or deny the fault encounter probability method presented here.

Another complication, however, is that while the Pond Fault is most simply interpreted and represented as a single fault, seismic sections suggest the subject offset may be due to a number of discrete, closely spaced faults (J. Wagoner, personal communication). The offset of such faults individually would of course be lower, so the density of such faults and the calculated probability of encountering them would be higher.

Also noteworthy is that the Pond Fault strikes northwest. This matches the primary orientation mode for faults in hydrocarbon fields centered between 16 km (10 mi.) and 24 km (15 mi.) from the site, but not the mode for faults in hydrocarbon fields centered within 16 km (10 mi.) of the injection site.

Fault Leakage Probability

The probability of leakage through a fault is a combination of that probability of the plume of concern encountering the fault and the probability of transmission along the fault. So

the probability of leakage through a fully seal offsetting fault is less than the probability of the plume encountering such a fault. For instance, shale-gouge ratio (SGR) research suggests that any point on a fault past which more than 20% of the rock that has been displaced is shale will tend to have near-shale, rather than near-reservoir-rock permeabilities (Yielding et al. 1996). By this theory, a fault that just fully offsets a seal consisting of 100% shale will have a minimum SGR of 50% adjacent to the overlying shale caprock, and therefore have low permeability. Consequently the probability of flow via this fault is less than 1, so the leakage probability is less than the encounter probability.

Conclusions

Fault population statistics allow estimation of the probability of a CO_2 plume (or displaced brine or pressure perturbation) encountering a fault of a particular size from available fault data. This is particularly useful when carrying out leakage risk assessment in the site-screening stage, or in the site evaluation stage, at sites with limited site-specific characterization of faults. One outcome of the application of this fault-population approach to fault encounter probability assessment is the realization that CO_2 plumes will encounter faults in most geologic sequestration environments because small-offset faults occur at high densities. This does not mean a priori that significant leakage will necessarily occur via these smaller faults, as evidenced by the persistence of buoyant hydrocarbon deposits frequently, if not typically, occurring in association with faulted terrain. This understanding should shift the consideration of leakage via faults from a more simple concern for plumes encountering faults, to a more detailed assessment of which faults are likely to be of concern, and what happens if the plume encounters those faults.

The probability of a plume encountering a fault is the first step in analyzing the risk of CO_2 (or brine) leakage via these potential pathways. The next probability concerns whether flow via a fault will occur. This is dependent on the flow and transport properties of the fault zone (permeability, relative permeability, porosity, residual saturation, capillary entry pressure, etc.). All of these probabilities are currently poorly constrained, which points out the need for further research characterizing these properties of faults and fractures, and development of tools to predict these properties with sufficient accuracy. Even still, given that uncertainties in fault-zone properties will always be present, methods such as probabilistic hazard analysis (PHA) may offer a useful approach for analyzing fault leakage risk.

This paper has described an approach and a result for fault intersection probability that is for a single project at a single stage in the process of site evaluation. If our result can be considered to have been validated, albeit in a very limited sense, based on subsequent findings at the site, it must be acknowledged that many such validation points are needed before any method in the data-limited field of reservoir characterization and engineering can be considered useful or not. Aggregation of such validation points across all or most projects would accelerate learning and facilitate assessment of capacity, impacts, and costs of large-scale geologic carbon sequestration. Sharing of characterization and performance information from each project at each stage is fundamental to any such effort.

Acknowledgments

We are grateful to Chris Doughty (LBNL) for sharing the Kimberlina Phase III pilot test simulation results, and to Jeff Wagoner (LLNL) for sharing his expertise regarding the geology of the southern San Joaquin Valley, particularly in the vicinity of the Kimberlina site. We thank

Tiemi Onishi for providing an internal review. This said the authors take full responsibility for the data analysis and conclusions presented. This work was supported in part by the CO_2 Capture Project (CCP) of the Joint Industry Program (JIP), and by Lawrence Berkeley National Laboratory under U.S. Department of Energy Contract No. DE-AC02-05CH11231.

REFERENCES

Ackerman, R. V., R. W. Schlische and M. O. Withjack, 2001. The geometric and statistical evolution of normal fault systems: an experimental study of the effects of mechanical layer thickness on scaling laws. Journal of Structural Geology. 23, 1803-1819.

Benson, S. M., and P. Cook, 2005. Underground geological storage, in: Intergovernmental Panel on Climate Change Special Report on Carbon Dioxide Capture and Storage, P. Freund (coordinating author). Cambridge University Press, Cambridge, U.K., pp. 195-276.

Bloch, R. B., 1986. Ramp-style deposition of Oligocene marine Vedder formation, San JoaquinValley. California, AAPG Bulletin. 70, 4.

Cowie, P. A., D. Sornette and C. Vanneste, 1995. Multifractal scaling properties of a growing fault population. Geophysical Journal International. 122, 457-469.

Division of Oil Gas and Geothermal Resources (DOGGR), 1998. California Oil and Gas Fields, Volume 1. 507 p.

Graham, S. A. and L. A. Williams, 1985. Tectonic, Depositional, and Diagenetic History of Monterey Formation (Miocene), Central San Joaquin Basin, California. AAPG Bulletin. 69: 385-411.

Holzer, T. L., 1980. Faulting caused by groundwater level declines, San Joaquin Valley. California.Water Resources Research. 16, 1065-1070.

Jordan, P.D., C.M. Oldenburg, and J.P. Nicot, 2010. Measuring and modeling fault density for plume-fault encounter probability estimation. Submitted to the AAPG Bulletin.

Los Angeles Department of Water and Power, 1974. San Joaquin nuclear project, early site review report. 5 volumes.

McPherson, B. A., 1978. Sedimentation and trapping mechanisms in Upper Miocene Stevens and older turbidite fans of the southeastern San Joaquin Valley, California. AAPG Bulletin. 62, 2243-2274.

Marrett, R. and R. W. Allmendinger, 1991. Estimates of strain due to brittle faulting: sampling of fault populations. Journal of Structural Geology. 13, 735-738.

National Energy Technology Laboratory (NETL), 2009. West Coast Regional Sequestration Partnership – development phase. 4 p. http://www.netl.doe.gov/publications/factsheets/project/Proj596.pdf accessed on June 9, 2009.

Oldenburg, C. M., S.L. Bryant, and J.-P. Nicot, 2009. Certification Framework based on effective trapping for geologic carbon sequestration. Int. J. of Greenhouse Gas Control. 3, 444–457.

Pickering, G., J. M. Bull and D.J. Anderson, 1995. Sampling power-law distributions. Tectonophysics. 248, 1-20.

Pruess, K. and García, J., 2002. Multiphase flow dynamics during CO_2 disposal into saline aquifers. Environmental Geology. 42, 282 – 295.

Smith, T. C., 1983. Pond Fault, Northern Kern County. California Division of Mines and Geology Fault Evaluation Report FER-144, p. 1-12.

Sheirer, A. H. (Ed.), 2007. Petroleum systems and geologic assessment of oil and gas in the San Joaquin Basin Province, California. United States Geological Survey Professional Paper 1713.

Wagoner, J., 2009. 3D Geologic Modeling of the Southern San Joaquin Basin for the Westcarb Kimberlina Demonstration Project- A Status Report. Lawrence Livermore National Laboratory, LLNL-TR-410813.

Watterson, J., J. J. Walsh, P. A. Gillispie and S. Eaton, 1996. Scaling systematics of fault sizes on a large-scale range fault map. Journal of Structural Geology. 18, 199 – 214.

Yielding, G., B. Freeman, and D. T. Needham, 1996. Quantitative fault seal prediction. AAPG Bulletin. 81, 897 – 917.

Zhang, Y., C. M. Oldenburg, S. Finsterle, P. Jordan, and K. Zhang, 2009. Probability estimation of CO2 leakage through faults at geologic carbon sequestration sites, in: Gale, J., H. Herzog, and J. Braitsch (Eds.), Proceedings of the 9th International Conference on Greenhouse Gas Control Technologies (GHGT-9), 16-20 November 2008, Washington DC, USA, pp. 41-46.

Appendix 1: Calculating elliptical plume length perpendicular to a fault

An alternative to measuring *k* from an anticipated plume shape is to assume the plume margin is elliptical. This assumption allows the derivation of equations for exploring the sensitivity of probability to plume size, aspect ratio and orientation in environments where the plume is expected to elongate, such as dipping reservoirs and reservoirs with horizontal permeability anisotropy.

For elliptical plumes, *k* can be computed from the plume area, A_p, the length-to-width aspect ratio, *m*, and θ_f (the acute angle between the fault and the plume axis), using a parametric approach. The value of these variables measured from an actual or simulated plume, can be assumed, or can be varied to explore sensitivity of Pr(*g*) to different plume geometries.

The derivation of *k* for an ellipse follows these general steps.

1) The semimajor axis, *a*, and the semiminor axis, *b* are computed from the measured A_p and *m* to approximate the plume margin as an ellipse.
2) An equation for the elliptical angle, θ, in terms of the auxiliary circular angle, *t*, and *m* (also known as a parametric equation) is developed.
3) A parametric equation for the angle between the ellipse tangent and the semi-major axis, ϕ, is similarly developed.
4) Parametric equations for *x* and *y* on the ellipse are developed.
5) The parametric equation for the length of the elliptical radius, r_e, is developed.

6) The parameter for the point of tangency of the fault to the ellipse, t_t, is computed by setting ϕ equal to the angle between the fault and the semi-major axis, ϕ_f , in the equation for ϕ as a function of t and solving for t_t.
7) A formula for the angle between a fault perpendicular and the radius to the point of tangency on the ellipse, α , is developed.
8) The length of the elliptical radius to the point of fault tangency is computed using t_t. in the equation for , r_e.
9) The length of k is computed.

This derivation is carried out below.

Elliptical approximation of an actual or simulated plume

To approximate an actual or simulated plume with an elliptical margin, A_p the plume length, and the plume width must be measured. The length is divided by the width to give m. The approximation then proceeds. The dimensions, a and b, of the approximating ellipse can then be calculated as follows:

$$m = \frac{a}{b} \qquad \text{(A-1)},$$

which can be rearranged to

$$a = mb \qquad \text{(A-2)}.$$

The area of an ellipse is given by

$$A_p = \pi ab \qquad \text{(A-3)}.$$

Substituting Equation A-2 into Equation A-3, this equation becomes

$$A_p = \pi m b^2 \qquad \text{(A-4)},$$

which can be solved for *b* as

$$b = \sqrt{\frac{A_p}{\pi m}} \qquad \text{(A-5)}.$$

With *b* from Equation A-5, *a* can be computed from Equation A-2.

Parametric equation for θ

Figure A-1 shows the variables for derivation of the parametric equations for θ, ϕ, *x* and *y*, and r_e.

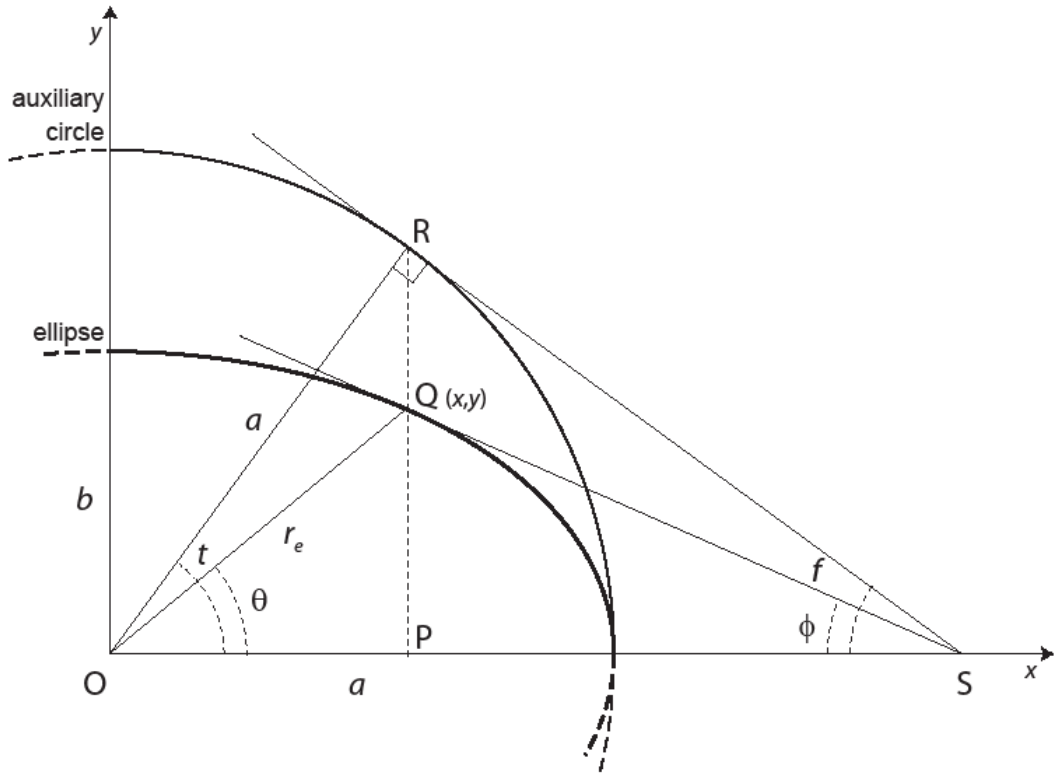

Figure A-1. Diagram of variables for the parametric definition of an ellipse.

The parametric equation for θ can be derived as follows. First,

$$\tan\theta = \frac{\overline{PQ}}{\overline{OP}} \qquad \text{(A-6).}$$

From compression of a circle to create an ellipse,

$$\overline{PQ} = \frac{1}{m}\overline{PR} \qquad \text{(A-7),}$$

and

$$\overline{PR} = \overline{OP}\tan t \qquad \text{(A-8).}$$

Substituting Equation A-8 into A-7 gives

$$\overline{PQ} = \frac{1}{m}\overline{OP}\tan t \qquad \text{(A-9).}$$

Substituting Equation A-9 into Equation A-6 and canceling terms yields

$$\tan\theta = \frac{1}{m}\tan t \qquad \text{(A-10).}$$

Solving for θ,

$$\theta = \tan^{-1}\frac{1}{m}\tan t \qquad \text{(A-11).}$$

Parametric equation for ϕ

The parametric equation for ϕ can be similarly derived as follows from

$$\tan\phi = \frac{\overline{PQ}}{\overline{PS}} \qquad \text{(A-12).}$$

Again,

$$\overline{PQ} = \frac{1}{m}\overline{PR} \qquad \text{(A-13),}$$

but for ϕ,

$$\overline{PR} = \overline{PS}\tan f \qquad \text{(A-14).}$$

From complementary angles,

$$f = \frac{\pi}{2} - t \qquad \text{(A-15).}$$

Substituting into Equation A-14,

$$\overline{PR} = \overline{PS}\tan(\frac{\pi}{2} - t) \qquad \text{(A-16).}$$

Using the identity

$$\tan(\frac{\pi}{2} - t) = \cot t \qquad \text{(A-17),}$$

and substituting into Equation A-16,

$$\overline{PR} = \overline{PS}\cot t \qquad \text{(A-18).}$$

Substituting into Equation A-13,

$$\overline{PQ} = \frac{1}{m}\overline{PS}\cot t \qquad \text{(A-19).}$$

Substituting into Equation A-12 and canceling terms, this equation becomes

$$\tan\phi = \frac{1}{m}\cot t \qquad \text{(A-20).}$$

Solving for ϕ,

$$\phi = \tan^{-1}\frac{1}{m}\cot t \qquad \text{(A-21).}$$

Parametric equations for point x, y on the ellipse

Deriving the *x* coordinate for a point on the ellipse at *t*,

$$x = \overline{OP} \tag{A-22}$$

and

$$\overline{OP} = a\cos t \tag{A-23}.$$

Therefore,

$$x = a\cos t \tag{A-24}.$$

Deriving the *y* coordinate for a point on the ellipse at *t*,

$$y = \overline{PQ} \tag{A-25},$$

$$\overline{PQ} = \frac{1}{m}\overline{PR} \tag{A-26},$$

and

$$\overline{PR} = a\sin t \tag{A-27}.$$

Substituting Equation A-27 into A-26 and canceling terms, the latter becomes

$$\overline{PQ} = b\sin t \tag{A-28}.$$

Substituting from Equation A-25

$$y = b\sin t \tag{A-29},$$

Parametric equation for r_e

The length of r_e is

$$r_e = \sqrt{x^2 + y^2} \qquad \text{(A-30).}$$

Substituting from Equations A-24 and A-29,

$$r_e = \sqrt{a^2 \cos^2 t + b^2 \sin^2 t} \qquad \text{(A-31).}$$

Parametric value at the point of fault tangency

Figure A-2 shows the variables for the remaining derivations.

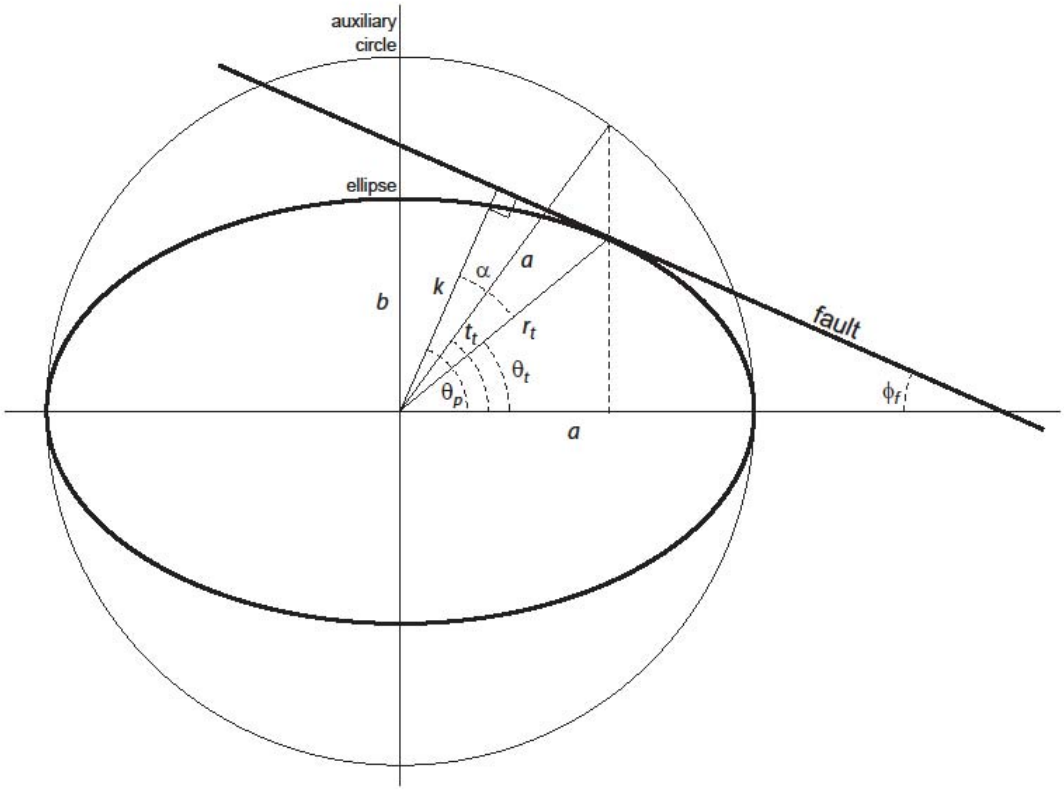

Figure A-2. Diagram for the derivation of the ellipse dimension perpendicular to a fault.

The value of t_t can be found by setting ϕ equal to ϕ_f in Equation A-21, and solving for t_t. From Equation A-21,

$$\phi_f = \tan^{-1} \frac{1}{m} \cot t_t \qquad \text{(A-32).}$$

Solving for t_t,

$$t_t = \cot^{-1} m \tan \theta_f \qquad \text{(A-33).}$$

Value of α

The value α is,

$$\alpha = \theta_p - \theta_t \qquad \text{(A-34)}$$

where θ_p is the angle between a normal to the fault and the semimajor axis, and θ_t is the elliptical angle at the point of fault tangency. From complementary angles,

$$\theta_p = \frac{\pi}{2} - \phi_f \qquad \text{(A-35).}$$

The value of ϕ_t can be found from Equation A-11 using t_t. Substituting this and Equation A-35 into Equation A-34 gives

$$\alpha = \frac{\pi}{2} - \phi_f - \tan^{-1} \frac{1}{m} \tan t_t \qquad \text{(A-36).}$$

Length of r_t

The value of r_t can be found from Equation A-31 using t_t:

$$r_t = \sqrt{a^2 \cos^2 t_t + b^2 \sin^2 t_t} \qquad \text{(A-37)}.$$

Length of k

The length of *k* can be computed from the following steps:

1) Compute *b* from A-5, if necessary.
2) Compute *a* from A-2, if necessary.
3) Compute t_t from A-33.
4) Compute α from A-36.
5) Compute r_t from A-37.
6) Compute *k* from

$$k = r_t \cos\alpha \qquad \text{(A-38)}.$$

The input values of A_p, *m*, and ϕ_f can be varied to determine the change in *k*, and the corresponding change in Pr(*g*).

FIGURE CAPTIONS

Figure 1. Diagram of 100 randomly located, circular plumes and a randomly located fault

Figure 2. Diagram of area containing the centers of circular plumes that will encounter the fault

Figure 3. Location of the Kimberlina Phase III pilot test in the San Joaquin Basin in California (modified from Sheirer 2007).

Figure 4. Oil and gas fields in the vicinity of the Kimberlina site. The Kimberlina site is at the star. North is up. (modified from DOGGR 1998)

Figure 5. Structure map of Calders Corner oil field. Elevations of fault blocks at fault intersections shown in large type. Interpolated fault throws in small italics.

Figure 6. Fault density versus throw truncation aggregated from the structure maps for the oil and gas fields shown on Figure 4. Exponential fit is shown.

Figure 7. Raw data shown as open symbols. Data corrected for the finite range effect shown in closed symbols. Linear fit to corrected data shown. Dashed lines are extrapolated from the linear fit.

Figure 8. Total CO_2 saturation and saturation in excess of residual from the numerical simulation. Total saturation is shown by contours. Saturation in excess of residual is shown by tints. Note the tints for saturation in excess of residual are defined on a log scale. Coordinates are in meters. North is up. (Courtesy of Christine Doughty, LBNL).

Figure 9. Probability that the Kimberlina plume will encounter a fault fully offsetting the seal. Open symbol represents the base case. Closed symbol represents a fault-biased permeability case. See Appendix 1 for computation method.

Figure 10. Probability that the Kimberlina plume will encounter a fault that offsets the seal at least halfway. Open symbol represents the base case. Closed symbol represents a fault-biased permeability case. See Appendix 1 for computation method.

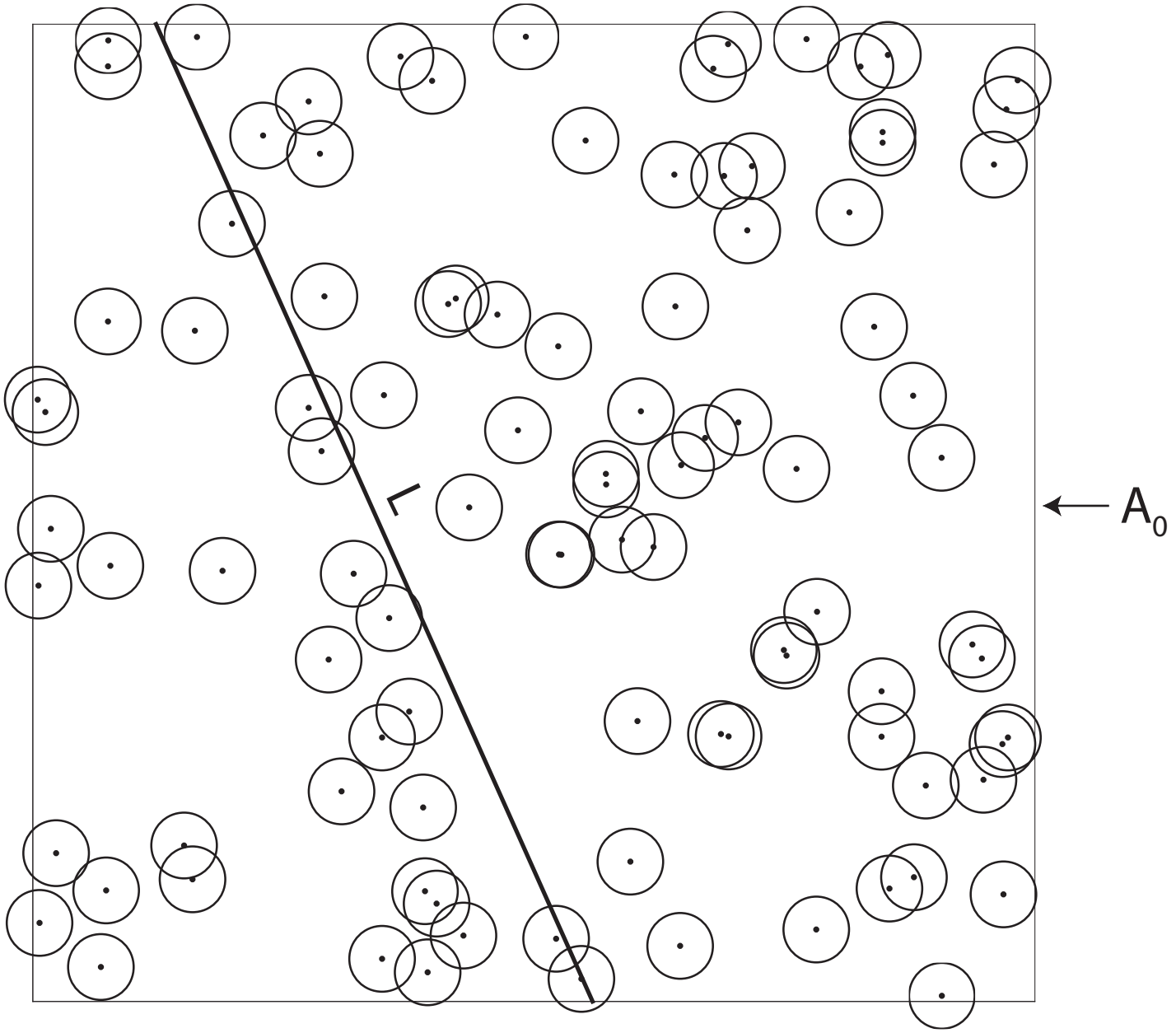

Figure 1

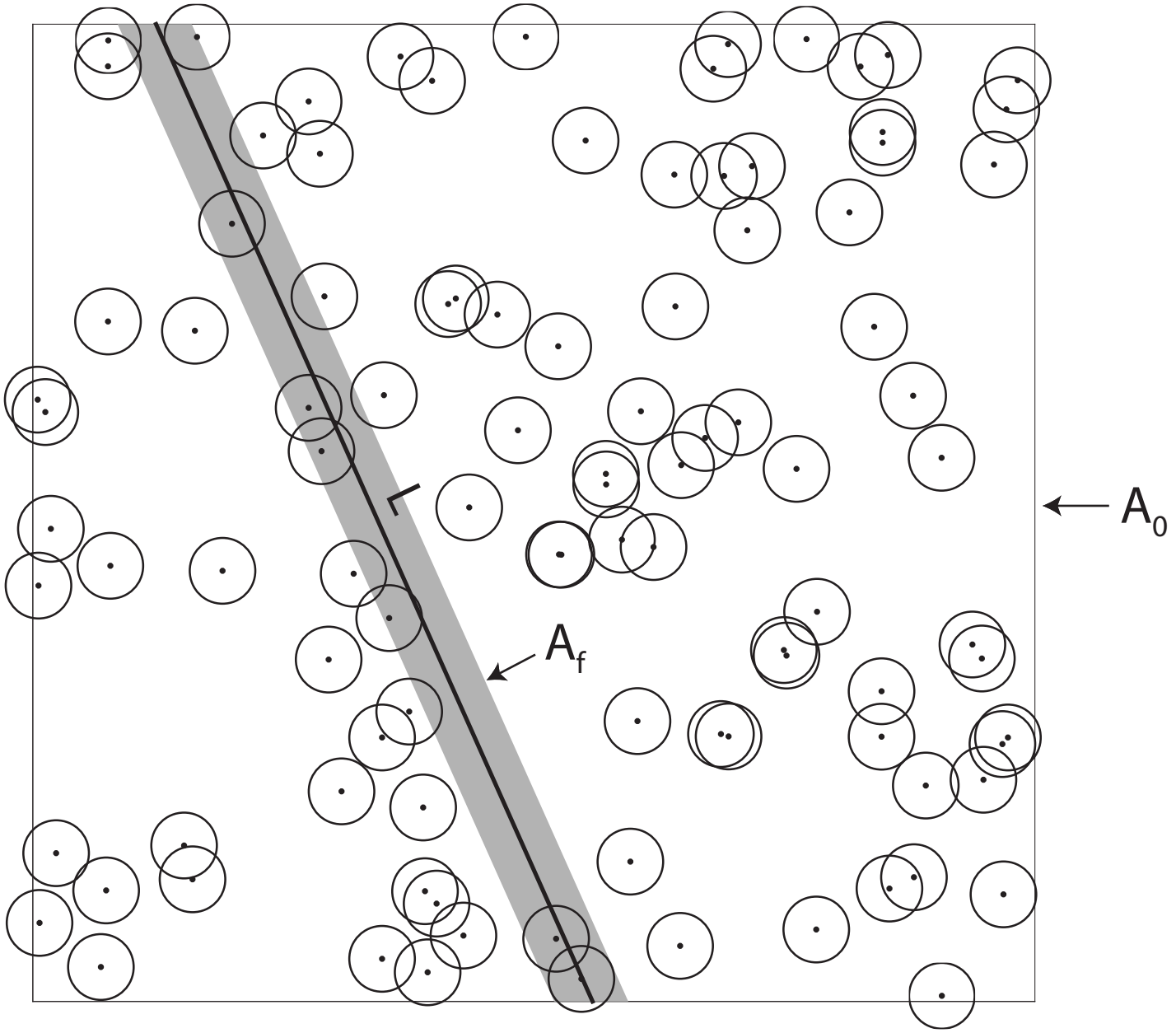

Figure 2

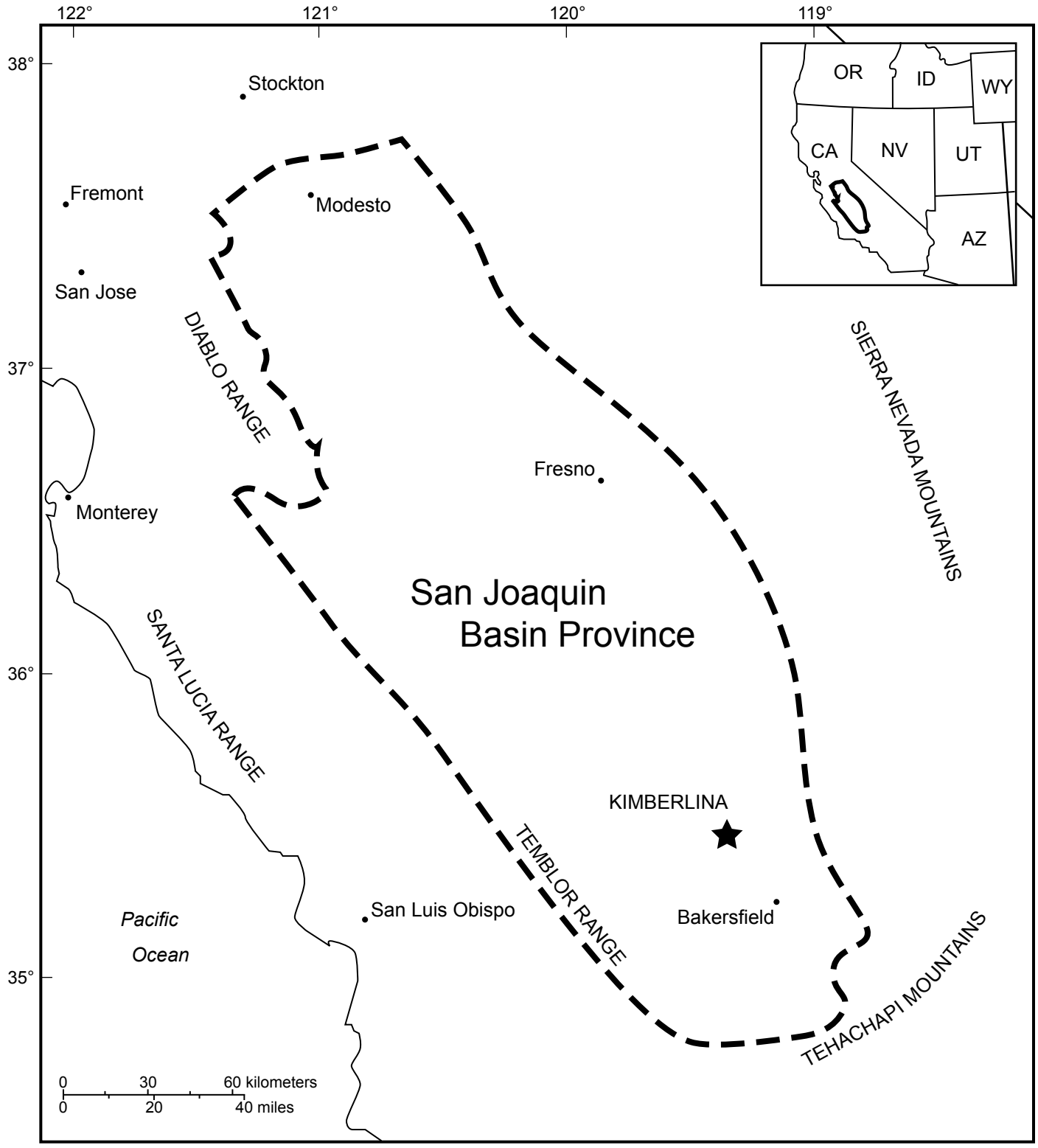
122°
121°
120°
119°
38°
37°
36°
35°
Stockton
Fremont
Modesto
San Jose
Monterey
Fresno
KIMBERLINA
San Luis Obispo
Bakersfield
Pacific
Ocean
DIABLO RANGE
SIERRA NEVADA MOUNTAINS
SANTA LUCIA RANGE
TEMBLOR RANGE
TEHACHAPI MOUNTAINS
San Joaquin
Basin Province
OR
ID
WY
CA
NV
UT
AZ
0 30 60 kilometers
0 20 40 miles

Figure 3

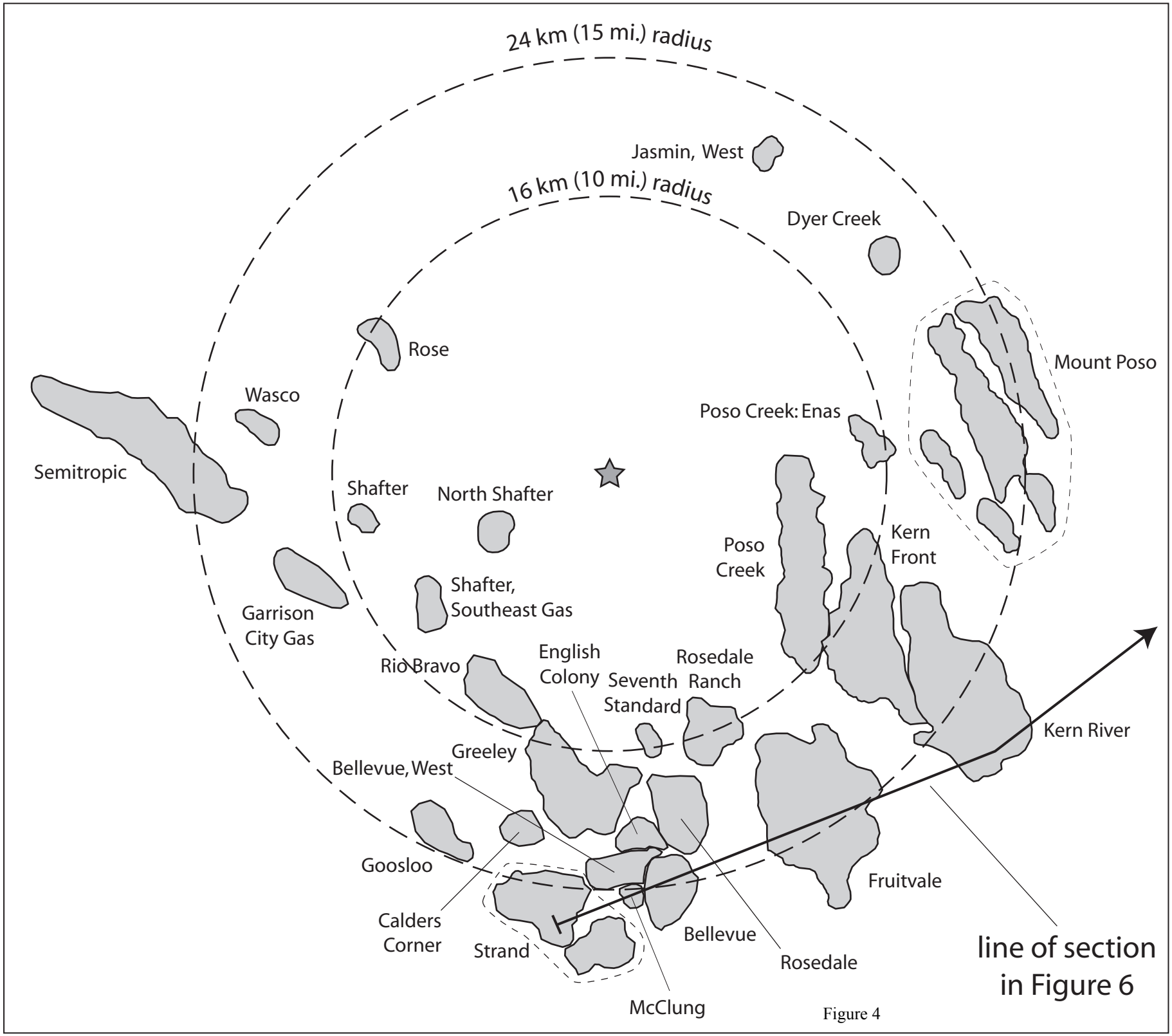
24 km (15 mi.) radius
16 km (10 mi.) radius
Jasmin, West
Dyer Creek
Rose
Mount Poso
Wasco
Poso Creek: Enas
Semitropic
Shafter
North Shafter
Poso
Creek
Kern
Front
Shafter,
Southeast Gas
Garrison
City Gas
English
Colony
Rosedale
Ranch
Rio Bravo
Seventh
Standard
Kern River
Greeley
Bellevue, West
Goosloo
Fruitvale
Calders
Corner
Strand
Bellevue
Rosedale
line of section
in Figure 6
McClung

Figure 4

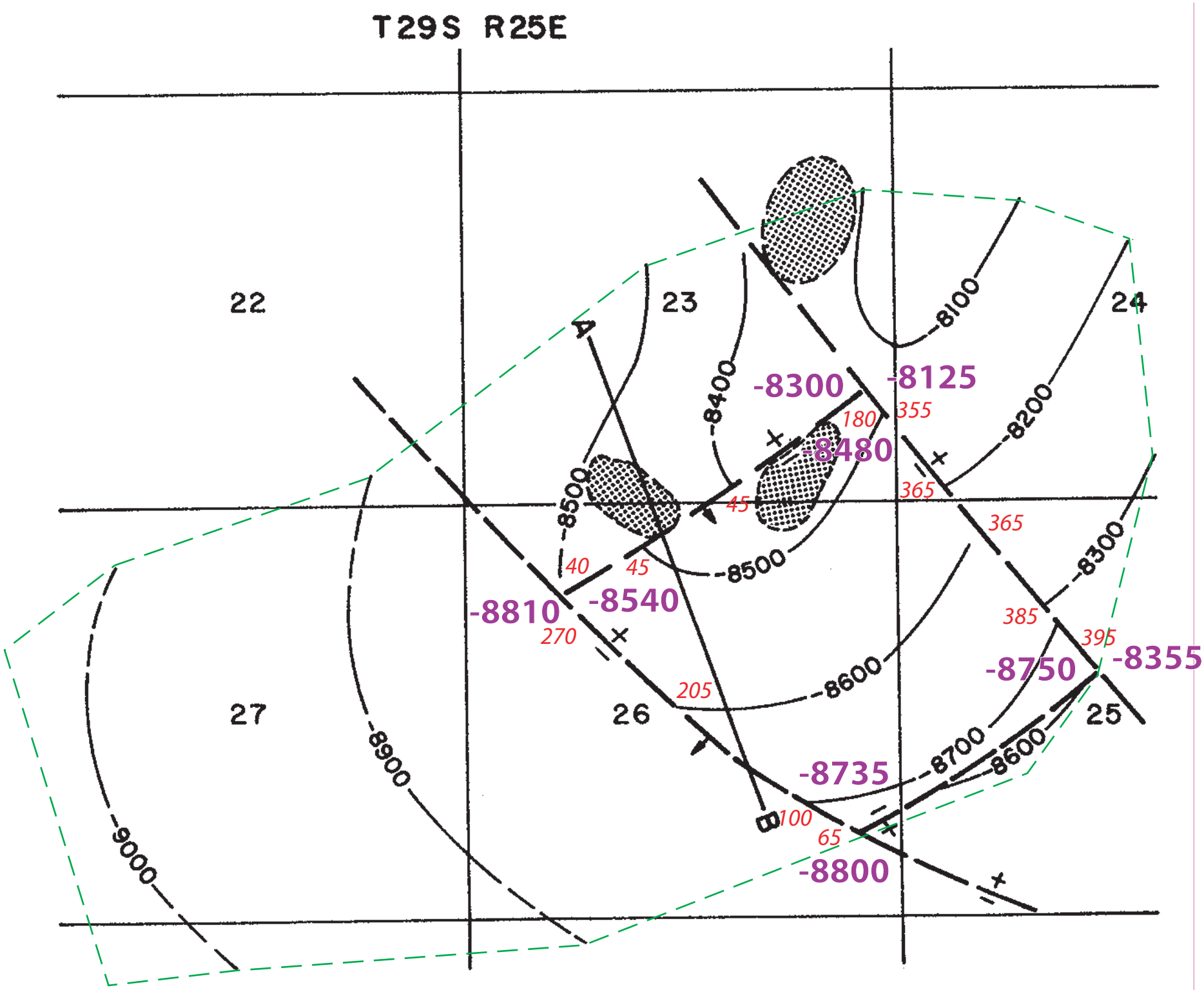

CONTOURS ON TOP OF STEVENS

Figure 5

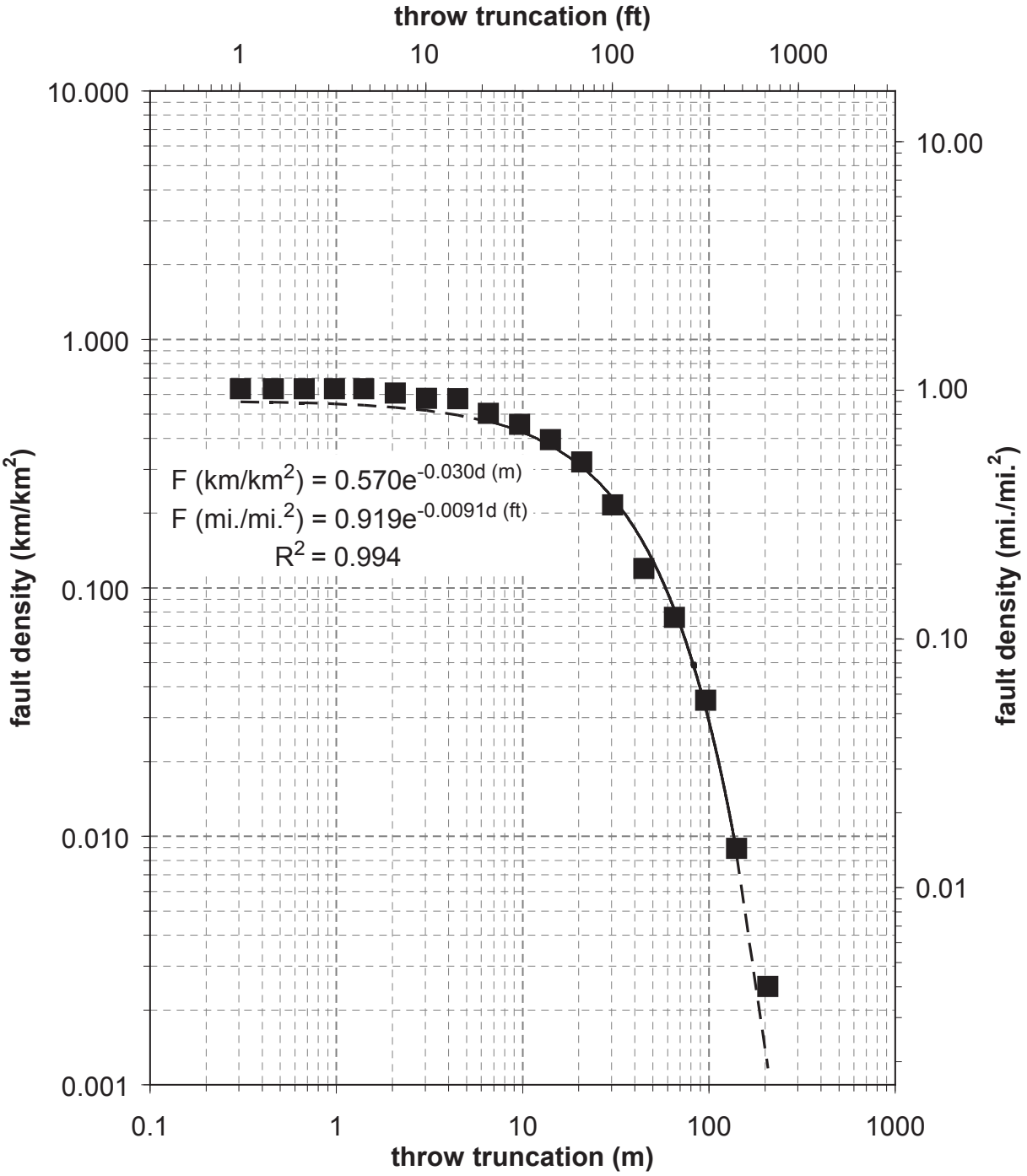
throw truncation (ft)
1
10
100
1000
10.000
1.000
0.100
0.010
0.001
10.00
1.00
0.10
0.01
fault density (km/km^2)
fault density (mi./mi.^{2})
F (km/km^2) = 0.570e$^{-0.030d\ (m)}$
F (mi./mi.^{2}) = 0.919e$^{-0.0091d\ (ft)}$
R^2 = 0.994
0.1
1
10
100
1000
throw truncation (m)

Figure 6

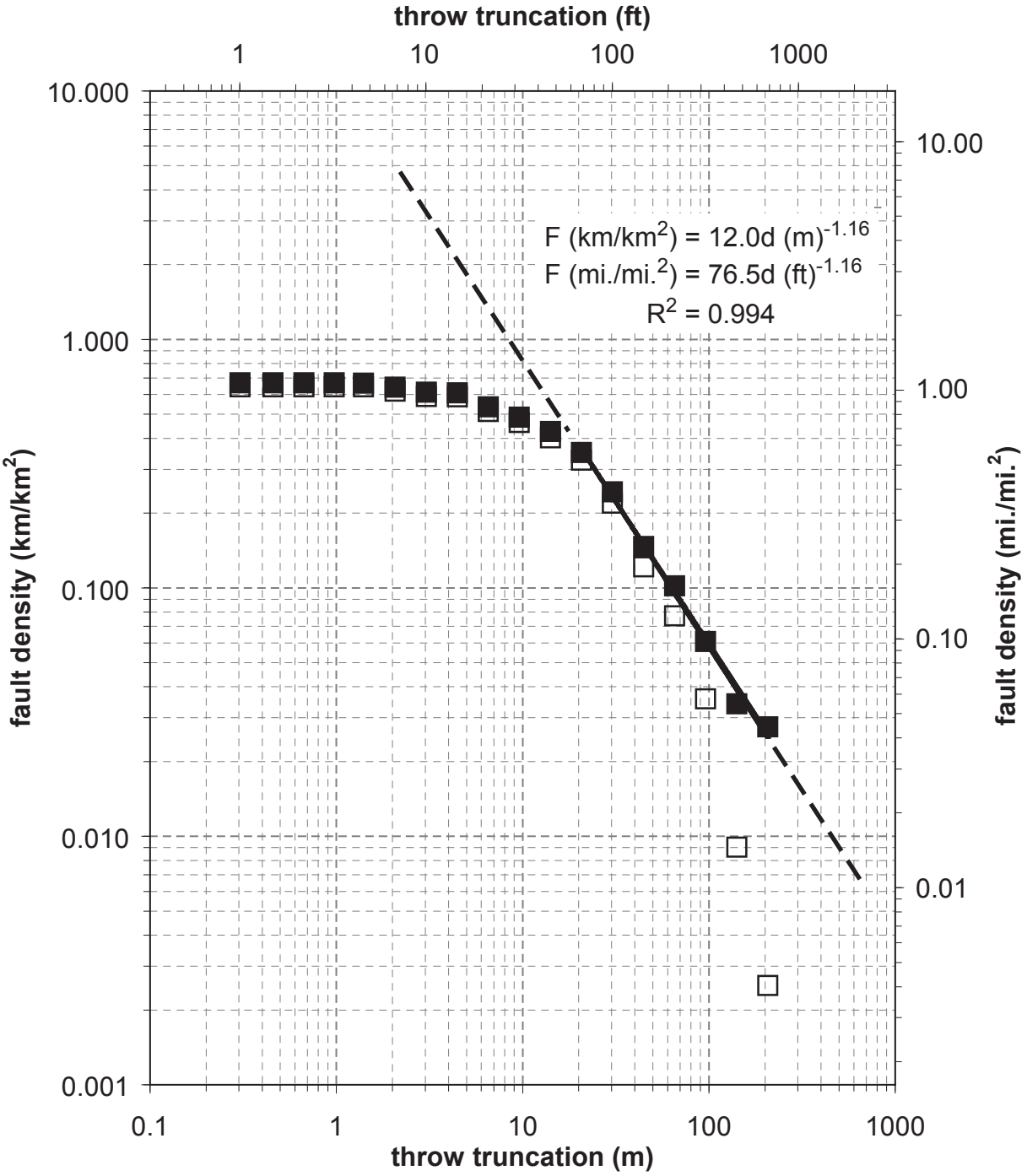
throw truncation (ft)
1
10
100
1000
10.000
1.000
0.100
0.010
0.001
10.00
1.00
0.10
0.01
F (km/km^2) = 12.0d (m)$^{-1.16}$
F (mi./mi.^{2}) = 76.5d (ft)$^{-1.16}$
R^2 = 0.994
fault density (km/km^2)
fault density (mi./mi.^{2})
0.1
1
10
100
1000
throw truncation (m)

Figure 7

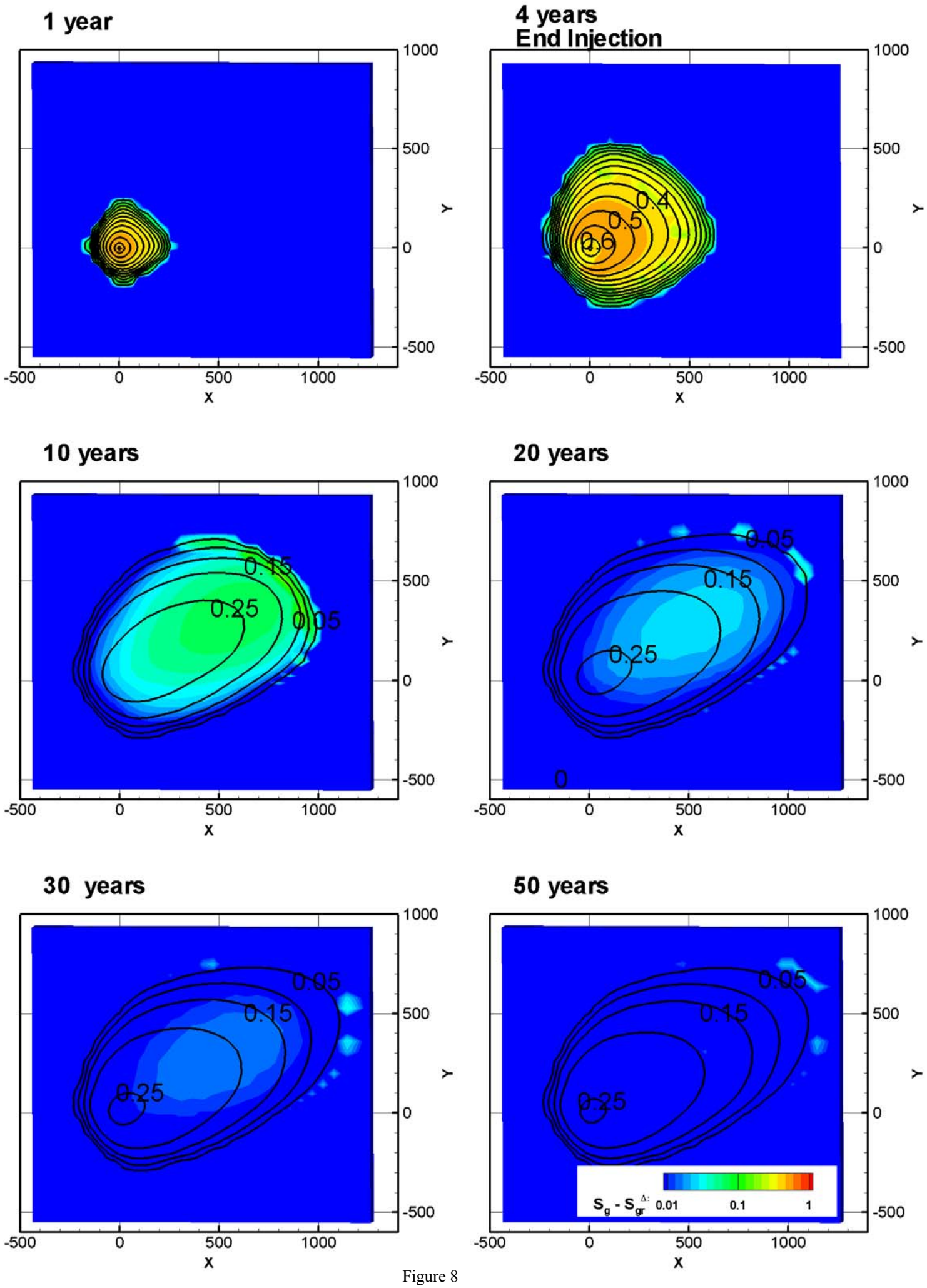
1 year
4 years
End Injection
10 years
20 years
30 years
50 years
0.4
0.5
0.6
0.15
0.25
0.05
0
$S_g - S_{gr}$
0.01
0.1
1
X
Y
-500
0
500
1000

Figure 8

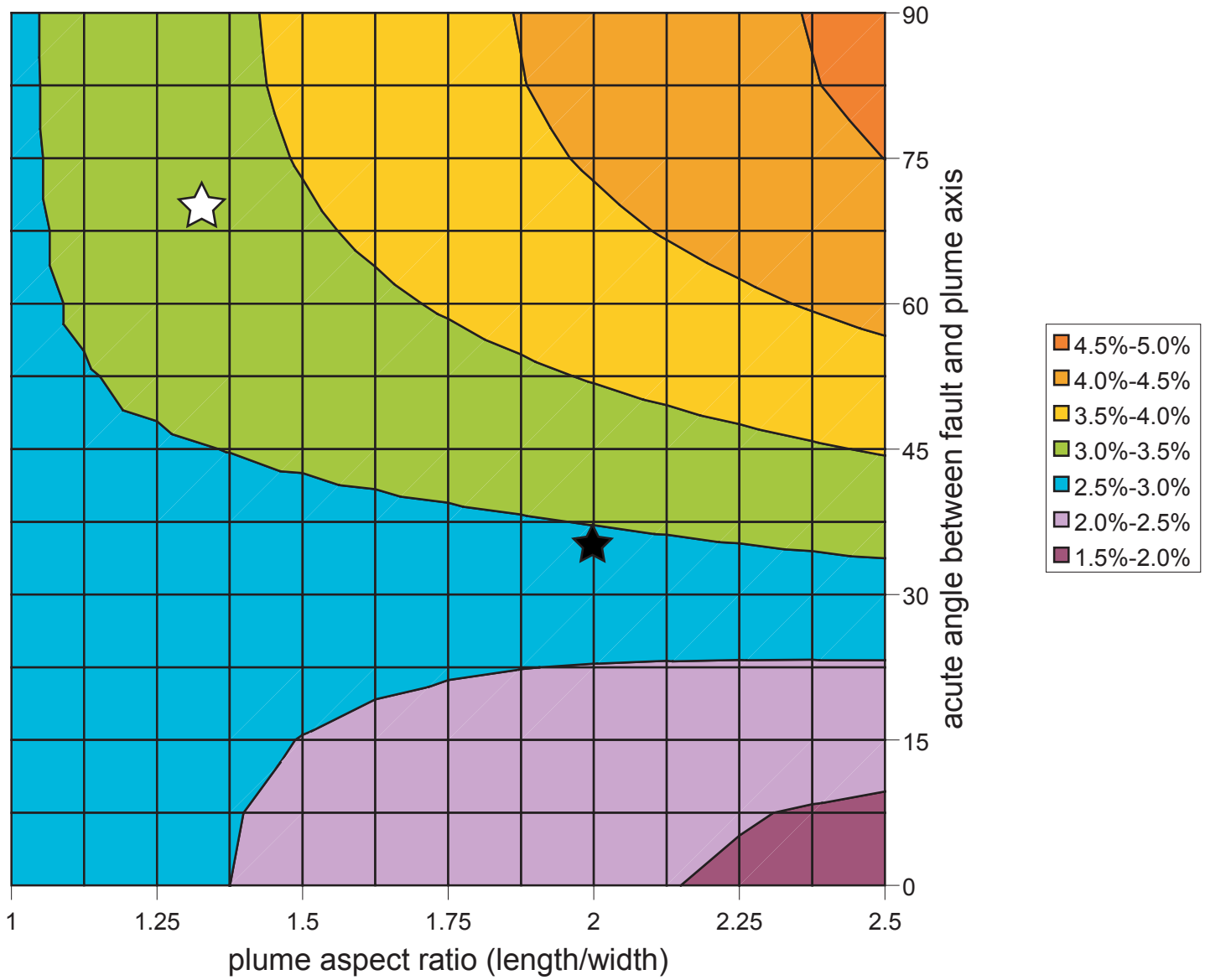
90
75
60
45
30
15
0
acute angle between fault and plume axis
1
1.25
1.5
1.75
2
2.25
2.5
plume aspect ratio (length/width)
4.5%-5.0%
4.0%-4.5%
3.5%-4.0%
3.0%-3.5%
2.5%-3.0%
2.0%-2.5%
1.5%-2.0%

Figure 9

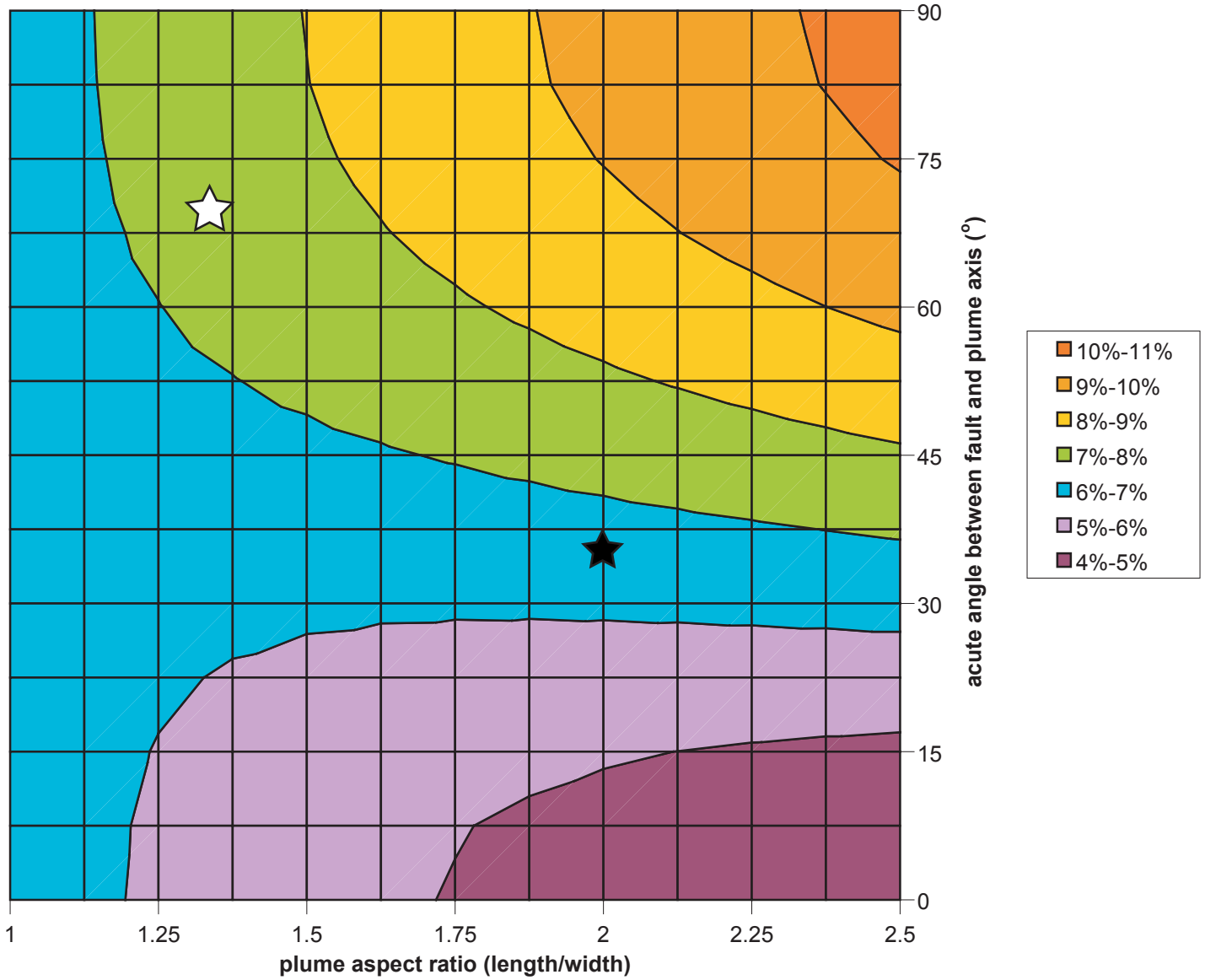
90
75
60
45
30
15
0
acute angle between fault and plume axis (°)
10%-11%
9%-10%
8%-9%
7%-8%
6%-7%
5%-6%
4%-5%
1
1.25
1.5
1.75
2
2.25
2.5
plume aspect ratio (length/width)

Figure 10

TABLES

Table 1. Probability of the Kimberlina mobile-CO_2 plume encountering a fully seal-offsetting fault for selected plume aspect ratios and plume axis to fault angles. Results calculated in part using the method in Appendix 1.

Plume axis to fault angle	Plume aspect ratio						
	1	**1.25**	**1.5**	**1.75**	**2**	**2.25**	**2.5**
0	2.9%	2.6%	2.4%	2.2%	2.1%	2.0%	1.9%
15	2.9%	2.7%	2.5%	2.4%	2.3%	2.2%	2.2%
30	2.9%	2.8%	2.7%	2.7%	2.7%	2.8%	2.8%
45	2.9%	3.0%	3.1%	3.2%	3.3%	3.4%	3.5%
60	2.9%	3.1%	3.3%	3.5%	3.7%	3.9%	4.1%
75	2.9%	3.2%	3.5%	3.8%	4.0%	4.3%	4.5%
90	2.9%	3.3%	3.6%	3.9%	4.1%	4.4%	4.6%

Table 2. Probability of the Kimberlina mobile-CO_2 plume encountering a fault that offsets the seal by at least half for selected plume aspect ratios and plume axis to fault angles. Results calculated in part using the method in Appendix 1.

Plume axis to fault angle	Plume aspect ratio						
	1	**1.25**	**1.5**	**1.75**	**2**	**2.25**	**2.5**
0	7%	6%	5%	5%	5%	4%	4%
15	7%	6%	6%	5%	5%	5%	5%
30	7%	6%	6%	6%	6%	6%	6%
45	7%	7%	7%	7%	7%	8%	8%
60	7%	7%	7%	8%	8%	9%	9%
75	7%	7%	8%	8%	9%	10%	10%
90	7%	7%	8%	9%	9%	10%	10%